The Astronomical Journal, 159:1 (14pp), 2020 January https://doi.org/10.3847/1538-3881/ab4da4
© 2019. The American Astronomical Society. All rights reserved.

An Updated Visual Orbit of the Directly Imaged Exoplanet 51 Eridani b and Prospects for a Dynamical Mass Measurement with *Gaia*

Robert J. De Rosa[1], Eric L. Nielsen[1], Jason J. Wang[2,34], S. Mark Ammons[3], Gaspard Duchêne[4,5], Bruce Macintosh[1], Julien Rameau[5,6], Vanessa P. Bailey[7], Travis Barman[8], Joanna Bulger[9,10], Jeffrey Chilcote[11], Tara Cotten[12], Rene Doyon[6], Thomas M. Esposito[4], Michael P. Fitzgerald[13], Katherine B. Follette[14], Benjamin L. Gerard[15,16], Stephen J. Goodsell[17], James R. Graham[4], Alexandra Z. Greenbaum[18], Pascale Hibon[19], Justin Hom[20], Li-Wei Hung[21], Patrick Ingraham[22], Paul Kalas[4,23], Quinn Konopacky[24], James E. Larkin[13], Jérôme Maire[24], Franck Marchis[23], Mark S. Marley[25], Christian Marois[15,16], Stanimir Metchev[26,27], Maxwell A. Millar-Blanchaer[7,35], Rebecca Oppenheimer[28], David Palmer[3], Jennifer Patience[20], Marshall Perrin[29], Lisa Poyneer[3], Laurent Pueyo[29], Abhijith Rajan[29], Fredrik T. Rantakyrö[19], Bin Ren[30], Jean-Baptiste Ruffio[1], Dmitry Savransky[31], Adam C. Schneider[20], Anand Sivaramakrishnan[29], Inseok Song[12], Remi Soummer[29], Melisa Tallis[1], Sandrine Thomas[22], J. Kent Wallace[7], Kimberly Ward-Duong[14], Sloane Wiktorowicz[32], and Schuyler Wolff[33]

[1] Kavli Institute for Particle Astrophysics and Cosmology, Stanford University, Stanford, CA 94305, USA
[2] Department of Astronomy, California Institute of Technology, Pasadena, CA 91125, USA
[3] Lawrence Livermore National Laboratory, Livermore, CA 94551, USA
[4] Department of Astronomy, University of California, Berkeley, CA 94720, USA
[5] Univ. Grenoble Alpes/CNRS, IPAG, F-38000 Grenoble, France
[6] Institut de Recherche sur les Exoplanètes, Département de Physique, Université de Montréal, Montréal, QC, H3C 3J7, Canada
[7] Jet Propulsion Laboratory, California Institute of Technology, Pasadena, CA 91109, USA
[8] Lunar and Planetary Laboratory, University of Arizona, Tucson, AZ 85721, USA
[9] Institute for Astronomy, University of Hawaii, 2680 Woodlawn Drive, Honolulu, HI 96822, USA
[10] Subaru Telescope, NAOJ, 650 North A'ohoku Place, Hilo, HI 96720, USA
[11] Department of Physics, University of Notre Dame, 225 Nieuwland Science Hall, Notre Dame, IN 46556, USA
[12] Department of Physics and Astronomy, University of Georgia, Athens, GA 30602, USA
[13] Department of Physics & Astronomy, University of California, Los Angeles, CA 90095, USA
[14] Physics and Astronomy Department, Amherst College, 21 Merrill Science Drive, Amherst, MA 01002, USA
[15] University of Victoria, 3800 Finnerty Road, Victoria, BC, V8P 5C2, Canada
[16] National Research Council of Canada Herzberg, 5071 West Saanich Road, Victoria, BC, V9E 2E7, Canada
[17] Gemini Observatory, 670 North A'ohoku Place, Hilo, HI 96720, USA
[18] Department of Astronomy, University of Michigan, Ann Arbor, MI 48109, USA
[19] Gemini Observatory, Casilla 603, La Serena, Chile
[20] School of Earth and Space Exploration, Arizona State University, P.O. Box 871404, Tempe, AZ 85287, USA
[21] Natural Sounds and Night Skies Division, National Park Service, Fort Collins, CO 80525, USA
[22] Large Synoptic Survey Telescope, 950 North Cherry Avenue, Tucson, AZ 85719, USA
[23] SETI Institute, Carl Sagan Center, 189 Bernardo Avenue, Mountain View, CA 94043, USA
[24] Center for Astrophysics and Space Science, University of California San Diego, La Jolla, CA 92093, USA
[25] NASA Ames Research Center, MS 245-3, Mountain View, CA 94035, USA
[26] Department of Physics and Astronomy, Centre for Planetary Science and Exploration, The University of Western Ontario, London, ON, N6A 3K7, Canada
[27] Department of Physics and Astronomy, Stony Brook University, Stony Brook, NY 11794-3800, USA
[28] Department of Astrophysics, American Museum of Natural History, New York, NY 10024, USA
[29] Space Telescope Science Institute, Baltimore, MD 21218, USA
[30] Department of Physics and Astronomy, Johns Hopkins University, Baltimore, MD 21218, USA
[31] Sibley School of Mechanical and Aerospace Engineering, Cornell University, Ithaca, NY 14853, USA
[32] Department of Astronomy, UC Santa Cruz, 1156 High Street, Santa Cruz, CA 95064, USA
[33] Leiden Observatory, Leiden University, 2300 RA Leiden, The Netherlands
Received 2019 April 11; revised 2019 October 10; accepted 2019 October 12; published 2019 December 10

Abstract

We present a revision to the visual orbit of the young, directly imaged exoplanet 51 Eridani b using four years of observations with the Gemini Planet Imager. The relative astrometry is consistent with an eccentric ($e = 0.53^{+0.09}_{-0.13}$) orbit at an intermediate inclination ($i = 136^{+10}_{-11}$ °), although circular orbits cannot be excluded due to the complex shape of the multidimensional posterior distribution. We find a semimajor axis of $11.1^{+4.2}_{-1.3}$ au and a period of $28.1^{+17.2}_{-4.9}$ yr, assuming a mass of 1.75 $M_{\odot}$ for the host star. We find consistent values with a recent analysis of VLT/SPHERE data covering a similar baseline. We investigate the potential of using the absolute astrometry of the host star to obtain a dynamical mass constraint for the planet. The astrometric acceleration of 51 Eri derived from a comparison of the *Hipparcos* and *Gaia* catalogs was found to be inconsistent at the 2σ–3σ level with the predicted reflex motion induced by the orbiting planet. Potential sources of this inconsistency include a combination of random and systematic errors between the two astrometric catalogs and the signature of an additional companion within the system interior to current detection limits. We also explored the potential of using *Gaia* astrometry alone for a dynamical mass measurement of the planet by simulating *Gaia* measurements of the

[34] 51 Pegasi b Fellow.
[35] NASA Hubble Fellow.

motion of the photocenter of the system over the course of the extended 8 yr mission. We find that such a measurement is only possible (>98% probability) given the most optimistic predictions for the *Gaia* scan astrometric uncertainties for bright stars and a high mass for the planet ($\gtrsim$3.6 $M_{\rm Jup}$).

Unified Astronomy Thesaurus concepts: Coronographic imaging (313); Astrometry (80); Exoplanet dynamics (490)

1. Introduction

The combination of relative astrometry of young, directly imaged substellar companions and absolute astrometry of their host stars is a powerful tool for obtaining model-independent mass measurements of this interesting class of objects (e.g., Brandt et al. 2019; Calissendorff & Janson 2018; Snellen & Brown 2018). At young ages, the luminosities of these objects encode information of their formation pathways (e.g., Marley et al. 2007), but interpretation is complicated by the degeneracy between initial conditions and the mass of the objects. While measurements from the ESA's *Gaia* satellite (*Gaia* Collaboration et al. 2016) will be used to discover thousands of planets via the astrometric reflex motion induced on the host star (Perryman et al. 2014), the vast majority of these detections will be around old stars where the observable signature of the initial conditions is lost, and photometric and spectroscopic characterization via direct imaging will be challenging if not prohibitively expensive. The intersection of these two techniques is giant planets and brown dwarfs detected around young ($\lesssim$100 Myr) and adolescent ($\lesssim$1 Gyr) nearby (<50 pc) stars. Their proximity increases the amplitude of the astrometric signal, allowing for a more precise mass measurement, and their youth allows for tight constraints on the bolometric luminosity (e.g., Chilcote et al. 2017), as well as detailed atmospheric characterization (e.g., Rajan et al. 2017).

The star 51 Eridani (51 Eri) is an F0IV (Abt & Morrell 1995) member of the 24–26 Myr (Bell et al. 2015; Nielsen et al. 2016) β Pictoris moving group (Zuckerman et al. 2001). The star is part of a wide hierarchical triple system with the M-dwarf binary GJ 3305 (Feigelson et al. 2006), with an ~60 kyr orbital period. As a nearby young star, 51 Eri was a prime target for direct imaging searches to identify wide-orbit self-luminous giant planets. Observations obtained with the Gemini Planet Imager (GPI; Macintosh et al. 2014) revealed a planetary-mass companion at a projected separation of 13 au (Macintosh et al. 2015). The mass of the planet derived from the observed luminosity is a strong function of the initial entropy of the planet after formation. Considering the extrema of plausible initial entropies, the planet has a mass of either 1–2 $M_{\rm Jup}$ for a high-entropy "hot-start" formation scenario or 2–12 $M_{\rm Jup}$ for a low-entropy "cold-start" scenario (Marley et al. 2007; Fortney et al. 2008). A measurement of the mass of the planet through a combination of relative and absolute astrometry would break this degeneracy, informing theories of giant planet formation at wide separations.

In this paper, we present a study of the orbital parameters of 51 Eri b and investigate whether a dynamical mass measurement or constraint can be made by combining relative astrometry from GPI with absolute astrometry from *Hipparcos* and *Gaia*. We describe our ground-based observations in Section 2 and present an updated visual orbit fit in Section 3. We use this fit to predict the astrometric signal induced by the orbiting planet on the host star and compare to measured values derived from a combination of the *Hipparcos* and *Gaia* catalogs in Section 4. We conclude with a prediction of the feasibility of a dynamical mass measurement of the planet using *Gaia* scan astrometry in Section 5.

2. Observations and Data Reduction

2.1. Data Acquisition and Initial Reduction

Under program codes GS-2015B-Q-501 and GS-2017B-Q-501, 51 Eri b has been observed periodically with the GPI (Macintosh et al. 2014) at Gemini South, Chile, during the Gemini Planet Imager Exoplanet Survey (GPIES; Nielsen et al. 2019a). The GPI combines a high-order adaptive optics system and an apodized coronagraph to achieve high-contrast, diffraction-limited imaging over a $2\farcs8 \times 2\farcs8$ field of view. This field is then sent into an integral field unit that disperses the light at each point within the field of view into a low-resolution spectrum ($\lambda/\Delta\lambda$ between 35 at Y and 80 at K). An observing log is given in Table 1; all observations were obtained in the default coronagraphic mode, but the filter and exposure time varied between epochs. All data sets were obtained in an angular differential imaging (ADI; Marois et al. 2006) mode with the Cassegrain rotator disabled, causing the field of view to rotate in the instrument as the target transits overhead. Short observations of an argon lamp (30 s) were obtained just prior to each science sequence to measure the positions of the microspectra in the raw frames that shift due to instrument flexure after large telescope slews. Observations of the arc were taken using the science filter, except for sequences using the K_1 and K_2 filters, where H was used instead to minimize calibration overhead. Longer sets of observations of the argon lamp (300 s) within each filter that are used for wavelength calibration, as well as darks of commonly used exposure times, are obtained periodically at zenith according to the observatory's calibration plan.

Data were reduced using the GPI Data Reduction Pipeline (DRP v1.5; Perrin et al. 2014), revision `a494dd5`, as a part of the GPIES automated data processing architecture (Wang et al. 2018b). Briefly, the DRP subtracts dark current, interpolates bad pixels using both a static bad pixel map and an outlier identification algorithm, constructs a three-dimensional (x, y, λ) data cube, corrects for distortion over the field of view, and measures both the location and the flux of the four satellite spots (attenuated replicas of the central star generated via diffraction off a wire grid in the pupil plane) within each of the 37 wavelength slices of the final reduced data cube. The location of the central star behind the coronagraph was estimated from the location of these satellite spots. Observations previously published in Macintosh et al. (2015) and De Rosa et al. (2015) were reduced using an earlier version of the pipeline that contained several errors affecting the parallactic angle calculation (De Rosa et al. 2019). These data were rereduced using the updated version of the pipeline to ensure consistency.

Table 1
51 Eri Gemini/GPI Observing Log and Associated KLIP Parameters

UT Date	Filter	N_{exp}	$t_{int} \times n_{coadds}$ (s)	Σt (minutes)	ΔPA (deg)	λ_{min}–λ_{max} (μm)	n_λ	m (pixels)	n_{KL}
2014 Dec 18[a]	H	38	59.6 × 1	37.8	23.8	1.508–1.781	35	2	50
2015 Jan 30[a]	J	45	59.6 × 1	44.7	35.1	1.130–1.334	35	2	50
2015 Jan 31[a]	H	63	59.6 × 1	62.6	36.5	1.509–1.779	35	2	50
2015 Sep 1[b]	H	93	59.6 × 1	92.5	43.8	1.512–1.777	35	2	50
2015 Nov 6	K_1	52	59.6 × 1	51.7	26.4	1.903–2.177	33	2.5	50
2015 Dec 18	K_2	103	59.6 × 1	102.4	71.8	2.131–2.316	25	2.5	50
2015 Dec 20	H	148	59.6 × 1	147.1	80.1	1.511–1.776	35	2	50
2016 Jan 28	K_1	97	59.6 × 1	96.4	55.5	1.941–2.172	28	2.5	50
2016 Sep 18	H	94	59.6 × 1	93.4	49.9	1.511–1.777	35	2	50
2016 Sep 21	J	83	29.1 × 2	82.5	53.1	1.133–1.332	35	1.5	50
2016 Dec 17	J	84	29.1 × 2	81.5	44.7	1.135–1.331	35	1.5	50
2017 Nov 11	H	44	59.6 × 1	43.7	27.7	1.508–1.777	35	2	50
2018 Nov 20	H	59	59.6 × 1	58.7	32.9	1.509–1.780	35	2	50

Notes.
[a] Rereduction of observations presented in Macintosh et al. (2015).
[b] Rereduction of observations presented in De Rosa et al. (2015).

2.2. PSF Subtraction

The reduced data cubes were further processed using the Karhunen–Loève image projection algorithm (KLIP; Soummer et al. 2012; Pueyo et al. 2015) to subtract the residual stellar halo that is not suppressed by the coronagraph and the forward model–based Bayesian KLIP-FM astrometry (BKA; Wang et al. 2016) to measure the astrometry of the companion within each data set. The forward model accounts for distortions in the instrumental point-spread function (PSF) caused by the PSF subtraction process, providing a better match between the models used to fit the location of the companion. We used the implementation of KLIP and BKA available as a part of the `pyKLIP` package[36] (Wang et al. 2015). Each wavelength slice of each data cube was high-pass-filtered prior to PSF subtraction to remove low spatial frequency signals such as the residual seeing halo and instrumental background at K. An instrumental PSF was then constructed at each wavelength by averaging the four satellite spots in time. Wavelength channels with low throughput in the K-band filters were discarded where the satellite spots were too faint. The wavelength range (λ_{min}–λ_{max}) and number of wavelength channels (n_λ) used for each data set are given in Table 1.

KLIP PSF subtraction was performed within a single annulus centered on the star with a width of 16 pixels at J and H and 20 pixels at K_1 and K_2 and a radius such that the companion was centered between the inner and outer bounds of the annulus. The two main tunable parameters in the PSF subtraction process are the exclusion criteria m, defining the number of pixels an astrophysical source must move before an image can be included in the PSF reference library, and the number of Karhunen–Loève modes n_{KL} used to reconstruct the stellar PSF. To explore the effects of the choice of these two parameters, we repeated the PSF subtraction using all combinations of $m \in \{1.0, 1.5, ..., 4.0\}$ and $n_{KL} \in \{1, 2, 3, 5, 10, 20, 50, 70\}$. The wavelength slices from each data cube after PSF subtraction were averaged, resulting in one final PSF-subtracted image per epoch. We calculated point-source sensitivity for each epoch and combined these into a single sensitivity map as a function of companion mass and semimajor axis using the algorithm described in Nielsen et al. (2013, 2019a), shown in Figure 1.

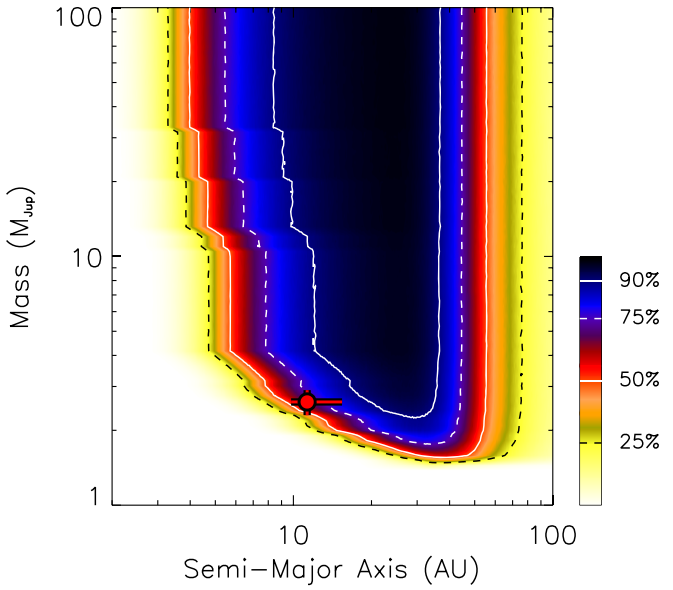

Figure 1. Sensitivity to companions of 51 Eri as a function of their mass and semimajor axis. Contours denote 25%, 50%, 75%, and 90% sensitivity calculated after marginalizing over all other orbital elements. We plot 51 Eri b using the mass derived from the H-band luminosity, the Baraffe et al. (2003) evolutionary models, and the Allard et al. (2012) substellar atmosphere models.

2.3. Relative Astrometry

The astrometry of the companion after each PSF subtraction of each epoch was then calculated using BKA. The forward model was created from the instrumental PSF given a specific combination of m and n_{KL} and fit to the companion within the PSF-subtracted image within a small 11 × 11 pixel box (or 15 × 15 pixels at K_1 and K_2) centered on the estimated location of the companion. Posterior distributions for the position and flux of the companion and the correlation length scale (Wang et al. 2016) were sampled using the Markov Chain Monte

[36] http://bitbucket.org/pyKLIP, revision `b3d97cd`.

Carlo (MCMC) affine-invariant sampler within the emcee package (Foreman-Mackey et al. 2013). For each fit, 100 walkers were initialized near the estimated location for each parameter and run for 800 steps, with the first 200 discarded as burn-in. Uncertainties in the star centering (0.05 pixels; Wang et al. 2014) and astrometric calibration (Table 2) from De Rosa et al. (2019) were combined in quadrature with the statistical uncertainty derived from the MCMC posterior distributions.

The choice of KLIP parameters was driven by many factors: the location of the companion, the amount of field rotation, the spatial distribution of noise within the residual images (Figure 2, fourth column), and the correlation (or lack thereof) between the KLIP parameters and the measured astrometry. Large values for the exclusion parameter m were preferred, although data sets with limited field rotation required a less restrictive setting. The parameters used for each data set are given in Table 1, and the astrometry derived from the data set processed with the selected parameters is given for each epoch in Table 2.

3. Updated Visual Orbit

The relative astrometry presented in Table 2 was used to refine the orbital parameters of the planet. We used the parallel-tempered affine-invariant MCMC sampler within the emcee package (Foreman-Mackey et al. 2013) to sample the posterior distributions of six orbital elements (semimajor axis a, eccentricity e, inclination i, argument of periastron ω, longitude of the ascending node Ω, and epoch of periastron τ), the parallax π, and the mass of the star M_1 and planet M_2. Rather than sampling ω and Ω individually, we sampled their sum ($\Omega + \omega$) and difference ($\Omega - \omega$) to speed up the convergence of the MCMC chains (Beust et al. 2014). Standard priors on the orbital parameters were adopted, uniform in $\log a$, e, and $\cos i$. Gaussian priors were adopted on π and M_1 based on the *Gaia* parallax measurement and uncertainties and literature estimates of the host star mass ($1.75 \pm 0.05\,M_\odot$; Simon & Schaefer 2011). Unlike systems where the period is constrained by the visual orbit (e.g., β Pic; Wang et al. 2016), we do not have sufficient coverage of the orbit to fit the total system mass directly, so we need to constrain the mass of the primary. We use a linear prior for M_2 between 1 and 15 $M_{\rm Jup}$, encompassing the range of masses predicted from the measured luminosity and evolutionary models (Macintosh et al. 2015; Rajan et al. 2017). The visual orbit alone only constrains the total system mass; additional information (e.g., radial velocities, absolute astrometry) is required to constrain the mass ratio and thus the masses of the two components.

We initialized 512 MCMC chains at each of 16 different temperatures (a total of 8192 chains). In the parallel-tempered framework, the lowest-temperature chains explore the posterior distributions of each parameter, while the highest-temperature chains explore the priors. Each chain was advanced for 10^6 steps and decimated, saving the position of each walker every tenth step. The first tenth of the final decimated chains were discarded as a "burn-in," where the location of the walkers was still a function of their initial position. The trimmed and decimated chains yielded a total of 46,080,000 samples at the lowest temperature.

The posterior distributions for six of the orbital elements are shown in Figure 3 and reported in Table 3, along with the minimum χ^2 and maximum probability (after accounting for the priors on the various parameters) orbits. We note that MCMC is not designed to find the minimum χ^2, and it is likely

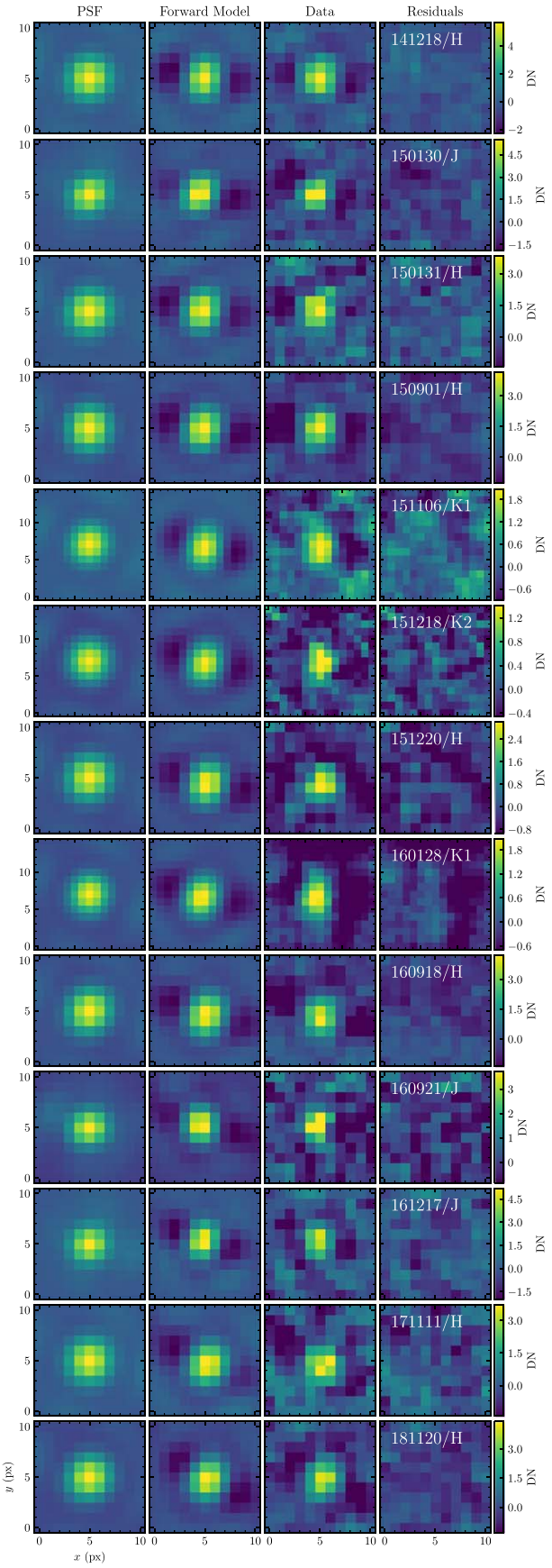

Figure 2. The GPI PSF (first column), BKA forward model (second column), companion (third column), and residuals (fourth column) for each 51 Eri observation. The KLIP parameters used for each reduction are given in Table 1.

Table 2
Relative Astrometry of 51 Eri b Using Bayesian KLIP Astrometry

UT Date	MJD	Instrument	Filter	Plate Scale (mas pixel^{-1})	North Offset (deg)	ρ (mas)	θ (deg)	Reference
2014 Dec 18	57,009.13	Gemini/GPI	H	14.161 ± 0.021	0.17 ± 0.14	454.24 ± 1.88	171.22 ± 0.23	1
2015 Jan 30	57,052.06	Gemini/GPI	J	14.161 ± 0.021	0.17 ± 0.14	451.81 ± 2.06	170.01 ± 0.26	1
2015 Jan 31	57,053.06	Gemini/GPI	H	14.161 ± 0.021	0.17 ± 0.14	456.80 ± 2.57	170.19 ± 0.30	1
2015 Feb 1	57,054.25	Keck/NIRC2	L'	9.952 ± 0.002	−0.252 ± 0.009	461.5 ± 23.9	170.4 ± 3.0	2
2015 Sep 1	57,266.41	Gemini/GPI	H	14.161 ± 0.021	0.17 ± 0.14	455.10 ± 2.23	167.30 ± 0.26	1
2015 Nov 6	57,332.23	Gemini/GPI	K_1	14.161 ± 0.021	0.21 ± 0.23	452.88 ± 5.41	166.12 ± 0.57	1
2015 Dec 18	57,374.19	Gemini/GPI	K_2	14.161 ± 0.021	0.21 ± 0.23	455.91 ± 6.23	165.66 ± 0.57	1
2015 Dec 20	57,376.17	Gemini/GPI	H	14.161 ± 0.021	0.21 ± 0.23	455.01 ± 3.03	165.69 ± 0.43	1
2016 Jan 28	57,415.05	Gemini/GPI	K_1	14.161 ± 0.021	0.21 ± 0.23	454.46 ± 6.03	165.94 ± 0.51	1
2016 Sep 18	57,649.39	Gemini/GPI	H	14.161 ± 0.021	0.32 ± 0.15	454.81 ± 2.02	161.80 ± 0.26	1
2016 Sep 21	57,652.38	Gemini/GPI	J	14.161 ± 0.021	0.32 ± 0.15	451.43 ± 2.67	161.73 ± 0.31	1
2016 Dec 17	57,739.13	Gemini/GPI	J	14.161 ± 0.021	0.32 ± 0.15	449.39 ± 2.15	160.06 ± 0.27	1
2017 Nov 11	58,068.26	Gemini/GPI	H	14.161 ± 0.021	0.28 ± 0.19	447.54 ± 3.02	155.23 ± 0.39	1
2018 Nov 20	58,442.21	Gemini/GPI	H	14.161 ± 0.021	0.45 ± 0.11	434.22 ± 2.01	149.64 ± 0.23	1

References. (1) This work; (2) De Rosa et al. (2015).

that orbits with slightly lower χ^2 could be found with a least-squares minimization algorithm using the best fit within the MCMC chains as a starting point. The quality of the fits to the astrometric record was typically good; the best-fit orbit had $\chi^2 = 13.4$, corresponding to $\chi^2_\nu = 0.67$ assuming 20° of freedom (M_1 and M_2 are dependent variables for a visual orbit fit), suggesting that the uncertainties on the astrometry were slightly overestimated. The visual orbit is plotted in Figure 4, showing the predicted track of the planet in the sky plane, as well as the change in the separation and position angle of the planet as a function of time.

With the additional three years of astrometric monitoring, we are beginning to constrain the eccentricity of the orbit of the planet. The fit presented in De Rosa et al. (2015) only marginally constrained the eccentricity relative to the prior, only excluding the highest eccentricities. We similarly exclude high eccentricities ($e > 0.86$ is excluded at the 3σ confidence level), but we also find that circular orbits are disfavored with the extended astrometric record. The preferred eccentricity is larger than for other directly imaged planets (e.g., Wang et al. 2018a; Dupuy et al. 2019), although the sample size is currently too small to say whether it is unusually large. Interestingly—and most likely coincidentally—the median of the eccentricity distribution is consistent with the mean eccentricity of wide-orbit ($P > 10^5$ days) stellar companions to early-type (A6–F0) stars (Abt 2005).

We find a marginally smaller semimajor axis of $11.1^{+4.2}_{-1.3}$ au with a significantly reduced uncertainty relative to De Rosa et al. (2015) and no significant change in the location and width of the inclination posterior distribution. There is a strong covariance between the eccentricity and inclination of the orbit: circular orbits are found closer to an edge-on configuration, while eccentric orbits are more face-on. A future radial velocity measurement of the planet has the potential to break this degeneracy well before continued astrometric monitoring is able to differentiate between the two families of orbits. In the context of additional undiscovered companions within the system, combining the semimajor axis and eccentricity distributions yields a periastron distance for the orbit of $r_{\rm peri} = 5.4^{+3.8}_{-1.7}$ au. The posterior distribution on the mass of the planet is not constrained whatsoever relative to the uniform prior distribution described previously.

3.1. Nonzero Eccentricity

The marginalized eccentricity posterior distribution shown in Figure 3 appears to suggest that circular orbits ($e \sim 0$) can be excluded at a high significance. This is in part due to the complex shape of the multidimensional posterior distribution. At small eccentricities, the inclination is tightly constrained to $125\overset{\circ}{.}2 \pm 0\overset{\circ}{.}8$, and the longitude of the ascending node Ω is similarly constrained to one of two specific angles ($164\overset{\circ}{.}3 \pm 0\overset{\circ}{.}4$ and $344\overset{\circ}{.}3 \pm 0\overset{\circ}{.}4$). At higher eccentricities, these two parameters are far less constrained. As a consequence, the volume of phase space with allowable orbits with $e \sim 0$ is considerably smaller than for more eccentric orbits despite the small difference in χ^2, shifting the marginalized posterior distribution toward noncircular orbits.

To investigate whether or not we could exclude a circular orbit based on the current astrometric record, we repeated the visual orbit fit described previously with the eccentricity and argument of periapse fixed at zero. We found a minimum χ^2 of 18.7, corresponding to $\chi^2_\nu = 0.85$, assuming 22° of freedom. This is not significantly different from the best-fit orbit found in the full fit described previously ($\chi^2_\nu = 0.67$). Using the Bayesian information criterion (BIC), a circular orbit is preferred with a $\Delta{\rm BIC} = 1.4$, but not at a significant level. We therefore cannot reject the possibility that 51 Eri b is on a circular orbit based on the current astrometric record, despite the shape of the marginalized posterior distribution shown in Figure 3.

3.2. Comparison with VLT/SPHERE Astrometry

Recently, Maire et al. (2019) published a revision to the orbital parameters based on a combination of literature astrometry and three years of VLT/SPHERE observations of the system. The posterior distributions for the orbital elements are consistent between the two studies; both show that highly eccentric orbits are excluded by the current astrometric record. Maire et al. (2019) noted a potential systematic offset between

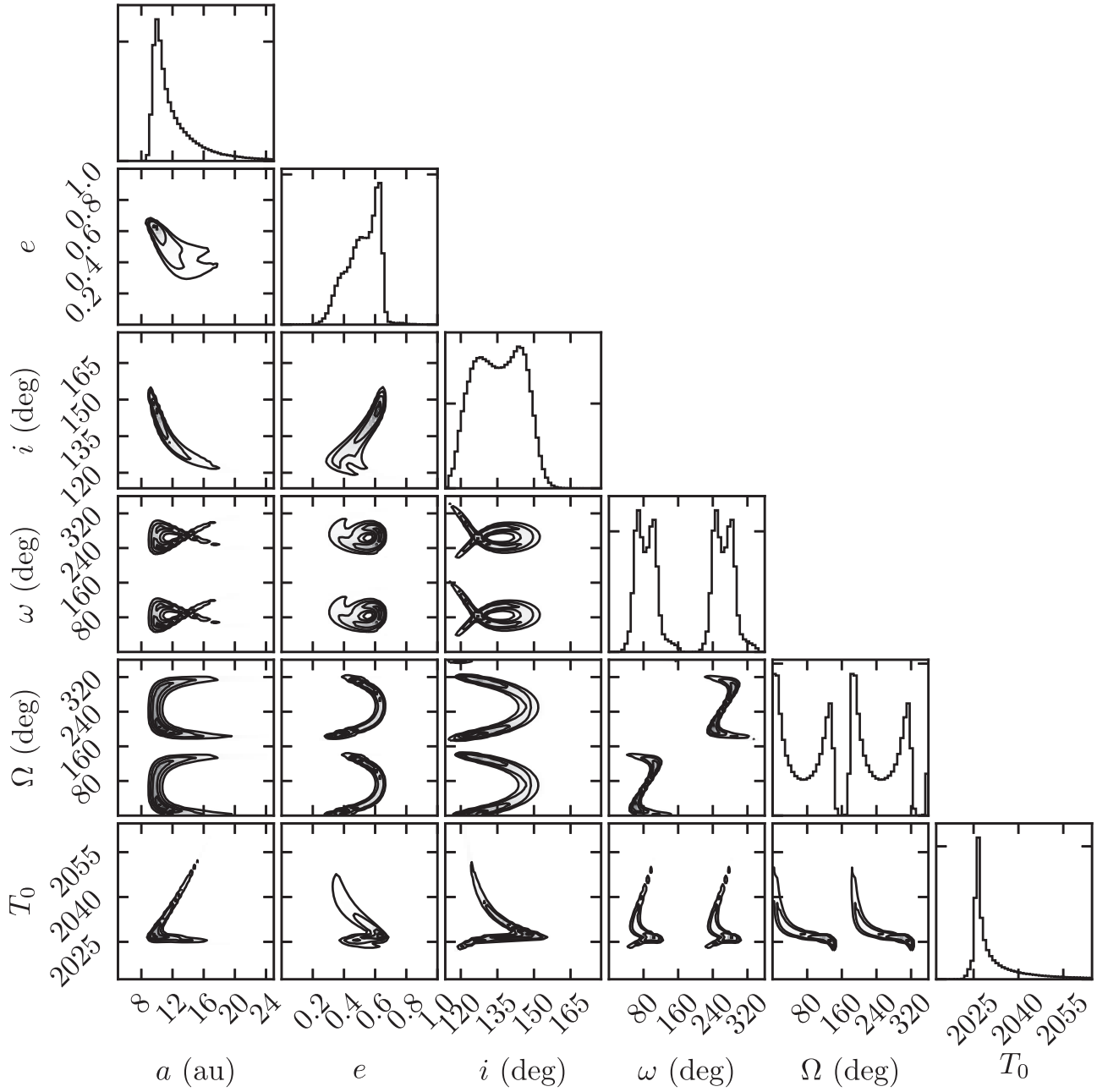

Figure 3. Posterior distributions and their covariance for six of the orbital elements for the visual orbit of 51 Eri b.

the position angle measurements from GPI and SPHERE of $\theta_{\rm SPH} - \theta_{\rm GPI} = \Delta\theta = 1\overset{\circ}{.}0 \pm 0\overset{\circ}{.}2$ based on an independent reduction of the GPI data available in the archive. The source of such an offset can be due to either a systematic offset in the determination of the true north angle for both instruments or an algorithmic issue caused by data reduction and/or post-processing.

We investigated this apparent discrepancy between the two instruments by performing a joint fit to the astrometry presented in Table 2 and Maire et al. (2019) with two additional parameters: a multiplicative term to describe a relative magnification $\rho_{\rm SPH}/\rho_{\rm GPI} = \Delta\rho$ and an additive term to describe a constant position angle offset $\Delta\theta$ applied to the GPI measurements. The orbit fit was performed as previously, although the chains were thinned by a factor of 100 rather than 10. Compared with the joint fit performed by Maire et al. (2019), we find a more marginal offset between the two instruments, with a magnification of $\Delta\rho = 1.0050 \pm 0.0047$ and a position angle offset of $\Delta\theta = -0\overset{\circ}{.}16 \pm 0\overset{\circ}{.}26$. We do not see any significant offset between the GPI and SPHERE astrometric records using the astrometry presented in Table 2 and Maire et al. (2019). This apparent discrepancy can be explained in part due to the revised astrometric calibration of GPI (De Rosa et al. 2019, submitted), in which the north offset angle was changed by several tenths of a degree relative to the original calibration used by Maire et al. (2019). Repeating the orbit fit using the astrometry from Table 2 but with the previous astrometric calibration yields a slightly different position angle offset of $\Delta\theta = 0\overset{\circ}{.}28 \pm 0\overset{\circ}{.}26$, significantly smaller than that found by Maire et al. (2019). This suggests that the difference in the measured position angle offset could be

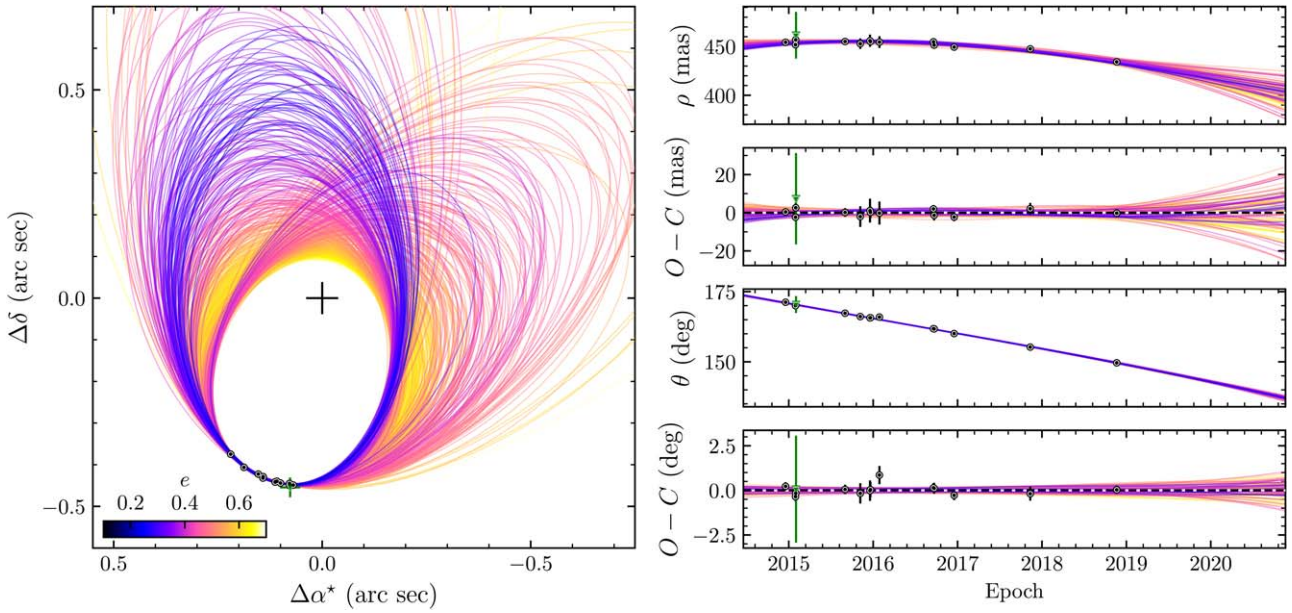

Figure 4. (Left) Five hundred visual orbits of 51 Eri b in the sky plane drawn from the MCMC chains, colored according to their eccentricity. Visual astrometry is overplotted from GPI (black) and NIRC2 (green). The location of the star is denoted by the plus sign. (Right) Evolution of the separation (first row) and position angle (third row) and their associated residuals.

Table 3
Campbell Elements and Associated Parameters Describing the Visual Orbit of 51 Eri b

Parameter	Unit	Median ($\pm1\sigma$)	Min. χ^2 Orbit	Max. $\mathcal{P}$ Orbit
P	yr	$28.1^{+17.2}_{-4.9}$	27.0	24.0
a	arcsec	$0.374^{+0.140}_{-0.044}$	0.363	0.338
a	au	$11.1^{+4.2}_{-1.3}$	10.8	10.1
$r_{\rm peri}$	au	$5.4^{+3.8}_{-1.7}$	4.7	3.9
e	⋯	$0.53^{+0.09}_{-0.13}$	0.57	0.61
i	deg	136^{+10}_{-11}	138.9	144.5
ω	deg	86^{+23}_{-23}[a]	108.3	285.3
Ω	deg	67^{+63}_{-56}[a]	116.0	282.4
τ	P	$0.56^{+0.18}_{-0.22}$	0.42	0.48
T_0	MJD	$61,735^{+4824}_{-712}$	61,143	61,202
T_0	yr	$2027.9^{+13.2}_{-2.0}$	2026.3	2026.4

Note.
[a] After wrapping Ω between 0° and 180°.

algorithmic in nature, rather than a systematic calibration offset between the two instruments.

4. Astrometric Acceleration

4.1. Absolute Astrometry and Inferred Acceleration

Astrometric measurements of 51 Eri were obtained from the rereduction of the *Hipparcos* catalog (van Leeuwen 2007a) and the second *Gaia* data release (DR2; *Gaia* Collaboration et al. 2018) and are given in Table 4. The *Gaia* catalog is known to suffer from a number of systematics for bright stars like 51 Eri. The uncertainties in the position, proper motion, and parallax were inflated based on the ratio of internal to external uncertainties estimated by the *Gaia* consortium (Arenou et al. 2018). The total

Table 4
Hipparcos and *Gaia* Absolute Astrometry of 51 Eri and Inferred Acceleration

Property	Unit	Value
Hipparcos (1991.25)		
HIP 21547		
α	deg	69.40044385 ± 0.29 mas[a]
δ	deg	−2.47339207 ± 0.20 mas
$\mu_{\alpha^\star}$	mas yr^{-1}	44.22 ± 0.34
μ_δ	mas yr^{-1}	−64.39 ± 0.27
π	mas	33.98 ± 0.34
Gaia (2015.5)		
Gaia DR2 3205095125321700480		
α (cat.)	deg	69.40074243852 ± 0.1067 mas[a]
α (corr.)	⋯	69.40074243852 ± 0.1163 mas[a,b]
δ (cat.)	deg	−2.47382451041 ± 0.0724 mas
δ (corr.)	⋯	−2.47382451041 ± 0.0798 mas[b]
$\mu_{\alpha^\star}$ (cat.)	mas yr^{-1}	44.352 ± 0.227
$\mu_{\alpha^\star}$(corr.)	⋯	44.395 ± 0.248[b]
μ_δ (cat.)	mas yr^{-1}	−63.833 ± 0.178
μ_δ (corr.)	⋯	−63.793 ± 0.196[b]
π (cat.)	mas	33.5770 ± 0.1354
π (corr.)	⋯	33.5770 ± 0.1477[b]
Inferred Proper-motion Difference		
$\mu_{\alpha^\star,\rm G} - \mu_{\alpha^\star,\rm H}$	mas yr^{-1}	0.174 ± 0.420
μ_δ, G−μ_δ, H	mas yr^{-1}	0.597 ± 0.334
$\mu_{\alpha^\star,\rm H} - \mu_{\alpha^\star,\rm HG}$	mas yr^{-1}	−0.065 ± 0.340
μ_δ, H−μ_δ, HG	mas yr^{-1}	−0.192 ± 0.270
$\mu_{\alpha^\star,\rm G} - \mu_{\alpha^\star,\rm HG}$	mas yr^{-1}	0.110 ± 0.249
μ_δ, G−μ_δ, HG	mas yr^{-1}	0.404 ± 0.197

Notes.
[a] Uncertainty in $\alpha^\star = \alpha \cos\delta$.
[b] After correcting for *Gaia* bright star reference frame rotation and the internal-to-external error ratio

uncertainty for each astrometric parameter was estimated using

$$\sigma_{\rm ext} = \sqrt{k^2\sigma_i^2 + \sigma_s^2}, \quad (1)$$

where σ_i is the catalog uncertainty, σ_s is a term representing the systematic uncertainty, and k is a correction factor applied to the internal uncertainty. For bright stars ($G < 13$), k is assumed to be 1.08, and σ_s is 0.016 mas for position, 0.021 mas for parallax, and 0.032 mas yr^{-1} for proper motion. Additionally, the bright star reference frame in the *Gaia* DR2 was found to be rotating with respect to the stationary extragalactic frame defined by distant quasars used for fainter stars. To correct for this, catalog proper motions were rotated by the rotation matrix given in Lindegren et al. (2018), with the catalog and rotation matrix uncertainties propagated using a Monte Carlo algorithm. Catalog and corrected values for the *Gaia* DR2 astrometry are given in Table 4; we exclusively used the corrected values for the analyses presented in this work.

We calculated three proper-motion differentials from the two catalogs. The first ($\mu_{\rm G}-\mu_{\rm H}$) was calculated simply as the difference between the proper-motion vector in the two catalogs ($\mu_{\rm H}$ for *Hipparcos* and $\mu_{\rm G}$ for *Gaia*). Nonrectilinear and perspective effects that cause a change in the apparent motion of nearby stars of constant velocity are negligible at the distance of 51 Eri ($\lesssim$1 μas yr^{-1}) and were therefore ignored. The two other differentials were calculated by comparing the instantaneous proper motion measured by each catalog ($\mu_{\rm H}$, $\mu_{\rm G}$) to the proper motion derived from the absolute position of the star in both catalogs ($\mu_{\rm HG}$). Uncertainties were calculated using a Monte Carlo algorithm. The three proper-motion differentials for 51 Eri are given in Table 2. A significant proper-motion difference was measured in the decl. direction for $\mu_{\rm G}-\mu_{\rm H}$ (1.8σ) and $\mu_{\rm G}-\mu_{\rm HG}$ (2.1σ); the other four values were not significantly different from zero.

4.2. Predicted Acceleration Due to 51 Eri b

We predicted the astrometric reflex motion induced by the orbiting planet on 51 Eri using the visual orbit fits described in Section 3. This signal was predicted using two different algorithms that produced consistent results. The first was based on the assumption that the *Hipparcos* and *Gaia* proper-motion measurements were instantaneous. This assumption is likely valid for *Gaia* due to the current wide separation of the planet but may not be valid for *Hipparcos* for more eccentric orbits. In this algorithm, the instantaneous proper motion of the photocenter was calculated at the reference epoch for both missions ($\mu_{\rm H}$, $\mu_{\rm G}$). The long-term proper motion ($\mu_{\rm HG}$) was calculated as the difference in the photocenter position at both epochs divided by the 24.25 yr baseline; a 10 mas shift in the position of the photocenter would manifest itself as a change in the proper motion of the star of $\sim$0.4 mas yr^{-1}. We assumed that the photocenter was centered on the host star; the planet contributes negligible flux within the *Hipparcos* and *Gaia* bandpasses.

The second algorithm was a simplistic simulation of the individual *Hipparcos* and *Gaia* measurements of the photocenter during the two missions. A simulated *Hipparcos* measurement was constructed by generating a one-dimensional abscissa measurement using a nominal set of astrometric parameters for the 51 Eri system barycenter. We adopted the *Hipparcos* catalog values, but the results should not be sensitive to small changes in the reference position, parallax, and proper motion of the system barycenter. The abscissa was constructed using the procedure described in Sahlmann et al. (2010) and the scan epochs, angles, and parallax factors for 51 Eri provided in the *Hipparcos* Intermediate Astrometric Data (IAD) catalog (van Leeuwen 2007b). The abscissa was perturbed by the predicted photocenter orbit for a given sample within the MCMC chains. The offset between the photocenter and system barycenter at each epoch in the $\alpha^\star$ and δ directions was weighted by the scan angle of the satellite at that epoch.

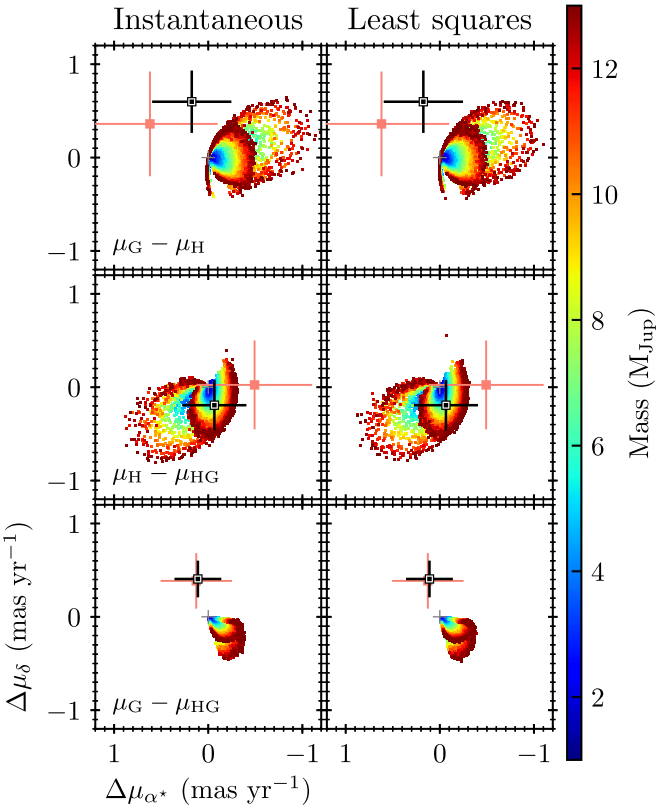

Figure 5. Predicted astrometric signal induced on 51 Eri by the orbiting planet from the instantaneous proper motion of the photocenter (left column) and the simplistic model of the *Hipparcos* and *Gaia* measurements (right column), both of which are calculated from the visual orbit fit. The colors of the symbols denote the mass of the planet for each visual orbit fit. For clarity, only 24,000 fits drawn randomly from the posterior distributions are plotted. The accelerations in Table 4 are plotted (black squares) in addition to those computed by Brandt (2018; red squares).

Using this simulated abscissa measurement, we predict what astrometric parameters would have been reported by *Hipparcos*. As the abscissa is a linear function of the five astrometric parameters ($\alpha^\star$, δ, π, $\mu_{\alpha^\star}$, μ_δ), a unique solution could be rapidly found through a simple matrix inversion. This allowed us to compute the five astrometric parameters that would have been measured by *Hipparcos* for each of the 4×10^7 orbits described in Section 3. This process was repeated to simulate a *Gaia* measurement of the motion of the photocenter using the scan epochs, angles, and parallax factors predicted for 51 Eri using the *Gaia* Observing Schedule Tool.[37]

4.3. Comparison with Measured Acceleration

The predicted proper-motion differentials calculated using these two algorithms are shown in Figure 5. The two

[37] https://gaia.esac.esa.int/gost/

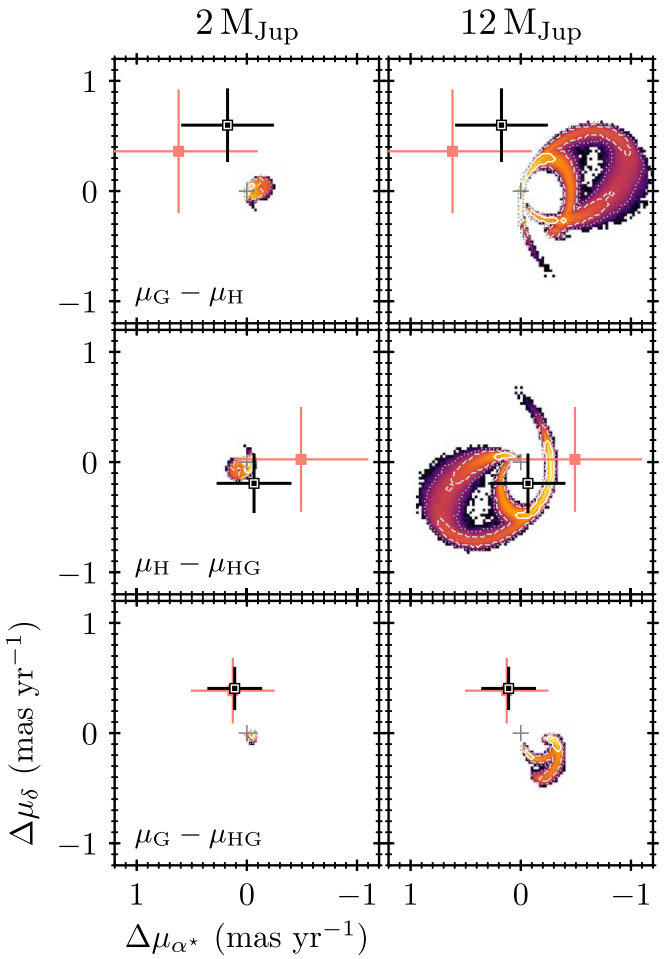

Figure 6. Predicted astrometric signal induced on 51 Eri by the orbiting planet derived from the simulated *Hipparcos* and *Gaia* measurements for a 2 $M_{\rm Jup}$ (left column) and 12 $M_{\rm Jup}$ (right column) planet. Contours denote 1σ, 2σ, and 3σ credible regions, and the color scale is the logarithmic count of the orbits within each bin of the two-dimensional histogram. The measured signal is denoted by the black symbol, and the accelerations computed by Brandt (2018) are also shown (red squares).

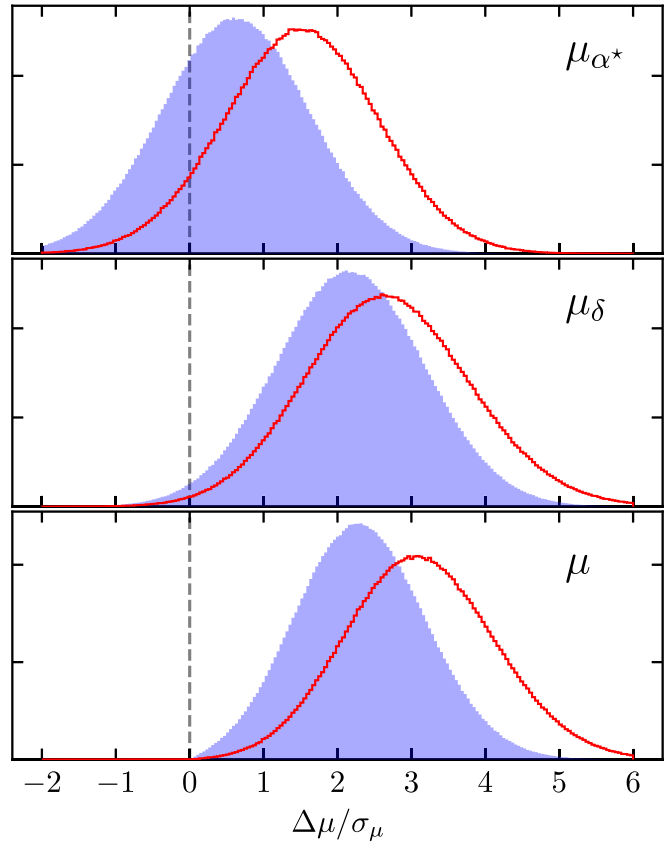

Figure 7. Distribution of the difference between predicted and measured $\mu_{\rm G} - \mu_{\rm HG}$ divided by the uncertainty on the measurement for low-mass (2 $M_{\rm Jup}$; blue filled histograms) and high-mass (12 $M_{\rm Jup}$; red open histograms) planets in the R.A. (top panel) and decl. (middle panel) directions and the total magnitude of the acceleration (bottom panel) assuming symmetric uncertainties on the measured acceleration.

algorithms are in excellent agreement, most likely due to the limited amount of curvature in the orbit of the photocenter during the *Hipparcos* and *Gaia* missions. The astrometric signal predicted using the second algorithm is plotted in Figure 6 for orbits with masses for the planet of 2.0 ± 0.5 and 12 ± 0.5 $M_{\rm Jup}$, corresponding to the range of plausible masses for the planet based on evolutionary models, drawn from the visual orbit MCMC fit. It is evident that there is a significant discrepancy between the predicted proper-motion differentials induced by the orbit of 51 Eri b and those measured with the *Hipparcos* and *Gaia* catalog values. The measured differential between *Gaia* and the long-term proper motion ($\mu_{\rm G}-\mu_{\rm HG}$) is notably discrepant; the direction of this acceleration is in the opposite direction predicted from the visual orbit, and the 1σ credible region for the predicted signal is significantly displaced from the measured value. A similar problem is seen for the difference between the two catalog proper motions ($\mu_{\rm H}-\mu_{\rm G}$), although both the measurement uncertainties and the 1σ credible interval of the predicted signal are larger. The two discrepant measurements both rely on the *Gaia* proper motion; the measured $\mu_{\rm H}-\mu_{\rm HG}$ acceleration is consistent with the predicted signal induced by 51 Eri b.

Recently, Brandt (2018) investigated potential systematic offsets between the *Hipparcos* and *Gaia* astrometric measurements and used a linear combination of the two *Hipparcos* reductions in an attempt to reduce observed discrepancies between the two catalogs. The revised proper motions presented within this catalog are not significantly different for 51 Eri (Figure 5, red symbols) and are virtually unchanged for the most discrepant of the three accelerations ($\mu_{\rm G}-\mu_{\rm HG}$).

Figure 7 shows the significance of the difference between the measured acceleration computed from the *Gaia* and long-term proper motions ($\mu_{\rm G}-\mu_{\rm HG}$) and that predicted from the visual orbit fit given in Section 3. The predicted acceleration from this combination of proper motions is the most constrained due to the relative astrometric record covering the same baseline as the *Gaia* mission. If we assume a mass of 2 $M_{\rm Jup}$ for 51 Eri b, the measured acceleration is 2.3σ discrepant (0.6σ and 2.2σ in the $\alpha^\star$ and δ directions), rising to 3.1σ (2.7σ and 1.5σ) for a 12 $M_{\rm Jup}$ planet.

The source of the discrepancy is not immediately apparent. When operating at the shortest integration times, 51 Eri ($G = 5.1$) is close to the nominal bright limit of the astrometric instrument ($G = 5$). The precision of the individual scan measurements at these magnitudes, between 1–2 mas along the scan direction, is 25–50 times worse than the formal Poissonian uncertainties (Lindegren et al. 2018). This difference was attributed primarily to inadequacies of the calibration models used to measure the centroid position of bright stars

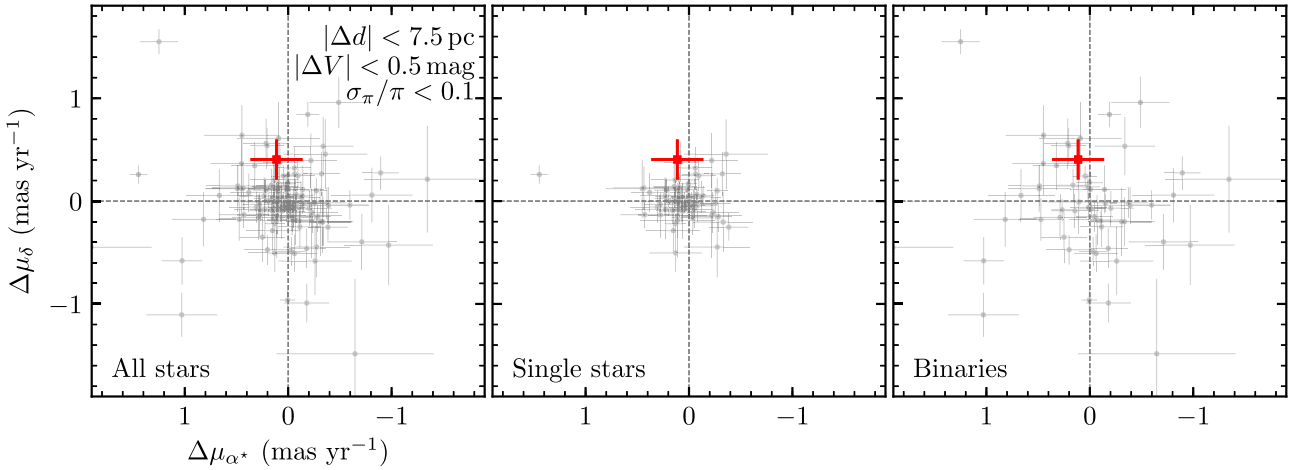

Figure 8. Astrometric acceleration measured between the *Gaia* and long-term proper motion for a sample of 155 stars (gray points) that share a similar distance, magnitude, and parallax uncertainty to 51 Eri (red). The three panels show the full sample (left), 71 single stars (middle), and 84 stars with evidence of binarity in the literature (right).

within each scan. It is not clear if these unmodeled errors would cause the centroid determination to be biased, or if they would simply introduce a random scatter on the measurement. It is plausible that the observed discrepancy is simply a random measurement error. This is more likely to be the case for a low-mass 51 Eri b, where the measurement is only a 2.3σ (roughly 1 in 40) outlier. If it is a measurement error, we are unable to differentiate between the low- and high-mass scenarios for the planet at a significant level due to the marginal difference in the distributions shown in Figure 7. The high-mass scenario is approximately 13 times less likely than the low-mass scenario (consistent with the relative probabilities in the mass posterior discussed at the end of this section) and cannot be excluded at a significant level with the available measurements.

The discrepancy could also be astrophysical in nature. An additional companion to 51 Eri interior to the current sensitivity limits of instruments such as GPI and SPHERE in an appropriate orbit could be inducing the observed astrometric signal, either entirely or in combination with 51 Eri b. As noted by Maire et al. (2019), a high eccentricity for the orbit of the planet could be the result of dynamical interactions with an additional companion within the system. To determine whether an astrophysical origin was a plausible source of the signal, we compared the measured $\mu_G - \mu_{HG}$ acceleration for 51 Eri to a sample of 155 stars at a similar distance ($|\Delta d| < 7.5$ pc), V-band magnitude ($|\Delta V| < 0.5$ mag), and *Hipparcos* parallax uncertainty ($\sigma_\pi/\pi < 0.1$). We found 51 Eri to be a 1.2σ outlier when comparing to all stars in the sample (Figure 8). However, the tails of the $\mu_G - \mu_{HG}$ distribution are undoubtedly contaminated with astrometric accelerations induced by stellar, substellar, and degenerate companions around these stars. We searched the Washington Double Star Catalog (Mason et al. 2001) to exclude binaries with a separation within 2″, the Ninth Catalog of Spectroscopic Binary Orbits (Pourbaix et al. 2004) to exclude spectroscopic binaries that can lead to spurious astrometric accelerations, and the Bright Star Catalog (Hoffleit & Jaschek 1991) for stars that had been categorized as being either variable radial velocity or a spectroscopic binary. We found evidence of binarity for 84 of the stars in the sample. Removing these binaries suppressed the tails of the distribution of astrometric accelerations for the 71 stars that to the best of our knowledge are single. The measured $\mu_G - \mu_{HG}$ acceleration for 51 Eri is more discrepant with this single subsample, a 1.5σ outlier, whereas it is consistent with the binary subsample. It is worth noting that not all of the stars within the single subsample have been searched for binary companions with either high-contrast imaging, interferometric observations, or radial velocity monitoring. The remaining outliers within this subsample are likely due to a combination of random measurement errors, systematic errors, and astrophysical signals induced by undiscovered companions.

These discrepancies have implications for an attempted measurement of the dynamical mass of 51 Eri b with a joint fit to the visual orbit of the companion and the absolute astrometry of the host star. Using the framework described in Nielsen et al. (2019b), we performed two fits to the available data. The first used all available astrometry of the planet and host star, and the second excluded the *Gaia* proper motion due to the observed discrepancy in Figure 5. Both fits utilized the *Hipparcos* IAD rather than the *Hipparcos* catalog values given in Table 4. The fit including the *Gaia* proper motion leads to a 1σ upper limit on the planet mass of $M_2 < 7\ M_{Jup}$, compared to $M_2 < 18\ M_{Jup}$ from the fit where it is excluded (Figure 9). Based on the discrepancy between the predicted and measured value of $\mu_G - \mu_{HG}$ (and to a lesser extent $\mu_H - \mu_G$), we cannot use the former mass constraint to confidently rule out a high-mass, low-entropy formation scenario for 51 Eri b. Instead, it is plausible that the fit is being driven toward to the lowest masses in an attempt to minimize the the $\mu_G - \mu_{HG}$ signal induced by the planet, which is in the opposite direction to the measurement. A similar discrepancy between the predicted and measured *Gaia* proper motions is seen for β Pic b (Nielsen et al. 2019b) and was not used to constrain the mass of that planet.

5. Future Mass Constraints with *Gaia*

The analyses presented in the previous sections are based on a comparison of the *Hipparcos* and *Gaia* catalog proper motions. These measurements represent the combination of $\sim 10^2$ individual astrometric measurements from each mission, fit based on an assumption of linear motion of the photocenter of the system. With sufficient astrometric precision, the reflex motion of the photocenter induced by the planet can be detected and used in conjunction with the visible orbit to constrain the mass of the planet. While the precision of the individual *Hipparcos* scan measurements ($\sigma = 1.0 \pm 0.3$ mas) is not

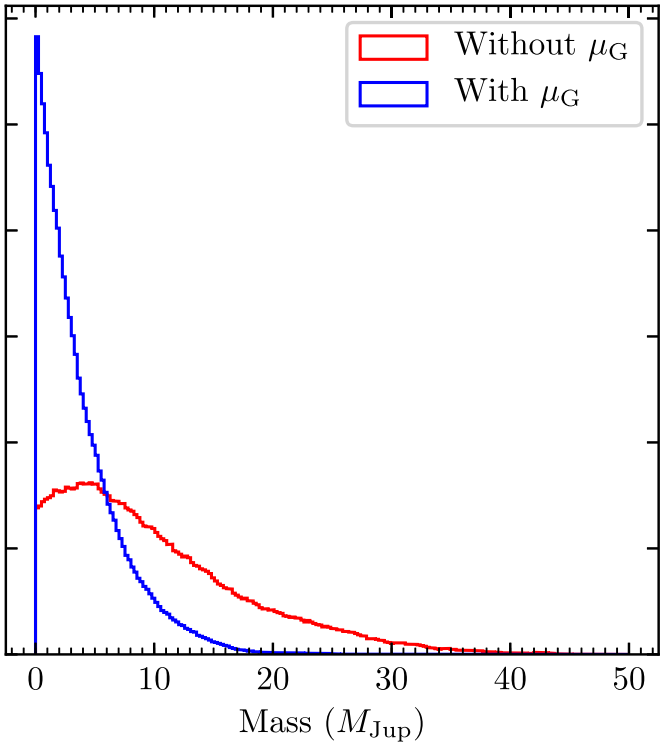

Figure 9. Posterior distributions for the mass of 51 Eri b from a joint fit to the relative and absolute astrometry of the system with (blue) and without (red) the *Gaia* proper motion.

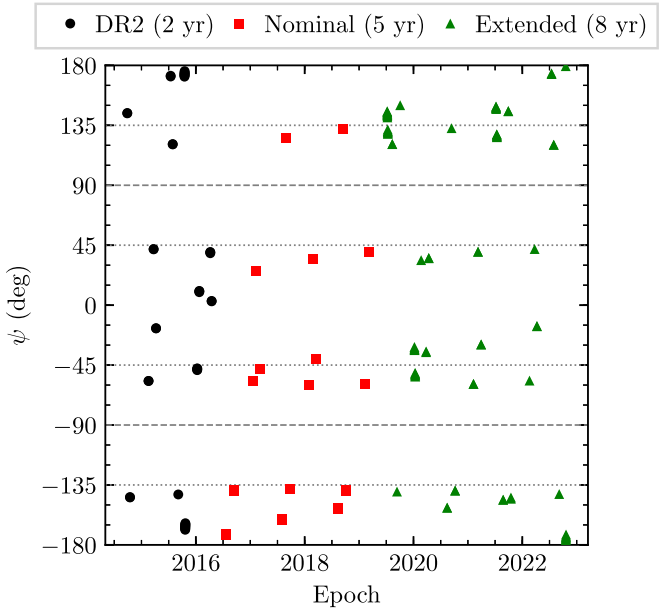

Figure 10. Scan angles for the *Gaia* measurements of 51 Eri b over the 2 yr used to construct the DR2 catalog (black circles), the nominal 5 yr mission (red squares), and an extended 8 yr mission (green triangles). A scan angle of $|\psi| = 90°$ (dashed lines) corresponds to a scan along the R.A. direction, constraining the position of the star only in that direction. Scan angles of $|\psi| = 45°$ and 135° (dotted lines) provide equal constraints on the position of the star along the two axes.

sufficient to measure the expected displacement of the photocenter over the 2.5 yr mission, the formal scan uncertainties for the final *Gaia* catalog are predicted to be significantly lower.

We utilized a similar framework to the one described in Section 4.2 to assess the potential of *Gaia* observations alone to constrain the mass of the planet. For the purposes of these simulations, we assumed that there is no additional massive companion within the system. We simulated a set of *Gaia* scan measurements of the 51 Eri system spanning three baselines, from the start of the mission (2014 July 25) to the end of the DR2 phase (2016 May 23), the end of the nominal 5 yr mission (assumed to be 2019 March 9), and the end of an extended 8 yr mission (assumed to be 2022 December 31). Predicted scan angles for the nominal and extended Gaia missions are shown in Figure 10.

Simulated abscissa measurements were generated by combining the linear motion of the 51 Eri barycenter with the orbital motion of the photocenter for each of the samples within the MCMC chains from Section 3. As with the model in Section 4.2, we assumed a nominal set of astrometric parameters for the system barycenter. Gaussian noise was added to the simulated measurements with an amplitude of either 50 μas, corresponding to the predicted noise floor for fifth-magnitude stars, or 250 μas, intermediate to this and the current median uncertainty of the individual scan measurements (Lindegren et al. 2018). Our noise model assumed that all of the measurements were uncorrelated. To assess whether the astrometric signal induced by the orbit of 51 Eri b would have been detected within each of these simulations, we fit the data with (1) a five-parameter model describing only the apparent motion of the system barycenter and (2) a 12-parameter model that also accounts for the motion of the photocenter due to the orbiting planet. The first fit is performed as described in Section 4.2. For the second fit, we used the framework described in Perryman et al. (2014). To speed up the optimization algorithm, we fix the period of the planet and only fit the two nonlinear terms u and v (transformed variables of the eccentricity e and mean anomaly at the reference epoch M_0); the linear terms are determined exactly for each (u, v) pair. We computed the χ^2 of each fit and considered the planet detected when $\Delta\chi^2 \geqslant 30$ (Perryman et al. 2014).

The distributions of $\Delta\chi^2$ as a function of the mass of the planet are shown in Figure 11 for the two noise models. We find that the astrometric signal induced by the planet is only detectable (>98% probability) in the simulations with the more favorable noise model (50 μas scan uncertainty) and planet masses of $M_2 \gtrsim 4\ M_{Jup}$ and that use the full data set from the extended 8 yr mission. The only possibility of an astrometric detection of 51 Eri b in the nominal 5 yr mission is if it was a $12\,M_{Jup}$ planet in a favorable orbital configuration, the highest mass predicted for the planet from the "cold-start" low-accretion formation scenario (Rajan et al. 2017). We predict that the astrometric signal of the planet will not be detectable at any plausible mass, assuming a per-scan uncertainty of 250 μas, which is already a factor of 4–8 improvement upon the estimate of the per-scan scan uncertainty of the astrometry used to create the *Gaia* DR2 catalog (Lindegren et al. 2018).

We also predicted the effect of an additional epoch of relative astrometry on the detectability of an astrometric acceleration with *Gaia*. We simulated one epoch of astrometry in 2021.9 consistent with an eccentricity at the median of the marginalized distribution ($e = 0.53$; $\rho = 357.1 \pm 3.0$ mas, $\theta = 129.^{\circ}1 \pm 0.^{\circ}3$) and used rejection sampling to select the orbits consistent with this measurement. The $\Delta\chi^2$ distribution for this subset of orbits is not significantly different; the planet is not detectable except in the most favorable circumstances. Repeating this analysis for a simulated measurement consistent with a low ($e = 0.40$) or high ($e = 0.62$) orbital eccentricity did

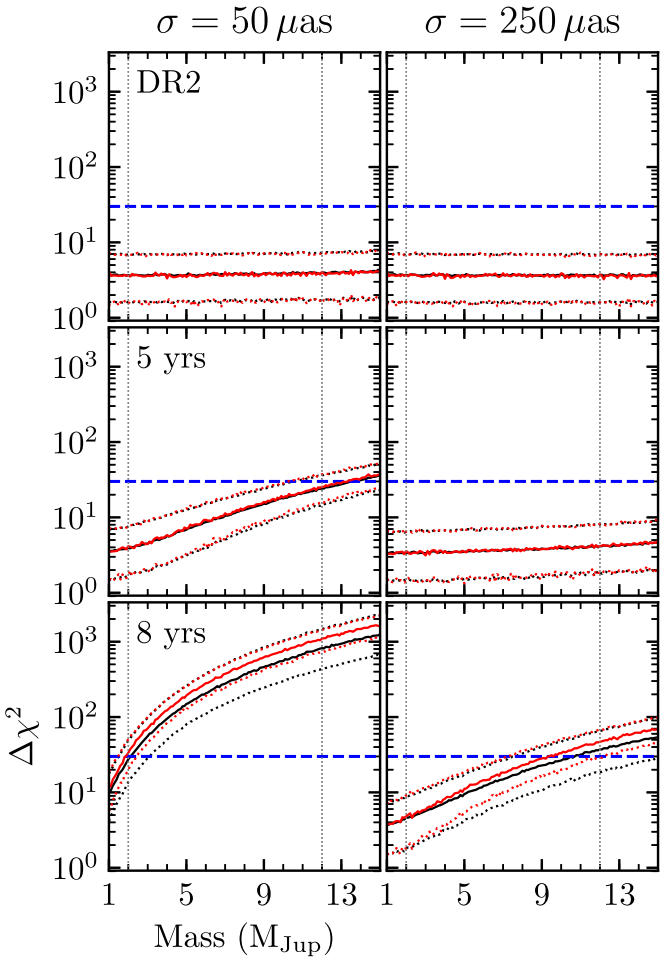

Figure 11. Median (solid lines) and 1σ range (dotted lines) of the $\Delta\chi^2$ between the five- and 12-parameter fits of the simulated *Gaia* abscissa measurements as a function of planet mass assuming a per-scan uncertainty of 50 (left column) and 250 (right column) μas. The fits were performed on simulated measurements spanning the DR2 epoch (top row), the nominal 5 yr mission (middle row), and the extended 8 yr mission (bottom row). The black curves are for the full set of visual orbits, and the red curves are for a subset of orbits consistent with a simulated epoch of relative astrometry in 2021.9. The model-dependent mass of the planet lies between 2 and 12 M_{Jup} (gray dotted lines), and the criterion for detection of $\Delta\chi^2 \geqslant 30$ is also shown (blue dashed line).

not lead to a significant change in the distribution of $\Delta\chi^2$ as a function of planet mass.

6. Conclusion

We have presented an update to the visual orbit of the young, low-mass, directly imaged exoplanet 51 Eri b using astrometry obtained with Gemini/GPI over the previous 3 yr. We find orbital elements that are consistent with an independent analysis of a data set combining literature GPI astrometry with new VLT/SPHERE measurements (Maire et al. 2019) and within the uncertainties presented in an earlier analysis with a 9 month baseline by De Rosa et al. (2015). We can confidently exclude a highly eccentric orbit for the planet, but a degeneracy exists between inclined low-eccentricity ($e \sim 0.2$) orbits and less inclined but more eccentric ($e \sim 0.5$) orbits. This degeneracy can be broken either with long-term astrometric monitoring of the visual orbit or in short order with a radial velocity measurement of the planet with instruments that combine high-contrast imaging techniques with high-resolution spectroscopy (e.g., Wang et al. 2017). Previous radial velocity measurements for short-period directly imaged exoplanets have used more traditional slit spectroscopy (Snellen et al. 2014), a technique that is challenging for 51 Eri b given the high contrast between the planet and its host star.

With a revised visual orbit for the system, we predicted the astrometric signal induced on 51 Eri by the orbiting planet and compared it to absolute astrometry from the *Hipparcos* and *Gaia* catalogs. We find that the predicted acceleration for the star due to the planet is inconsistent with the measured value at the 2σ–3σ level, and for one combination of catalog proper motions, the acceleration vector is in the opposite direction to that predicted by the visual orbit. This discrepancy could be due a combination of random measurement errors and other sources of uncertainty in the *Gaia* astrometry that have not been correctly modeled for bright stars (Lindegren et al. 2018) or a real astrophysical signal induced by an additional companion within the system that is interior to current detection limits. This discrepancy precludes a dynamical mass determination or constraint using the currently available data. Finally, we performed simulations of the individual *Gaia* scan measurements of 51 Eri over the course of the extended 8 yr *Gaia* mission. We demonstrated that a dynamical mass measurement of 51 Eri b using *Gaia* data alone is only possible at >98% confidence assuming the most optimistic predictions for the final per-scan uncertainty of the *Gaia* astrometry and a mass of $\gtrsim$4 M_{Jup} for the planet.

The upcoming *Gaia* data releases will contain astrometric accelerations, photometric orbit fits, and the individual scan measurements used to construct the catalog. Combined with long-term proper motions derived from *Hipparcos* positions (e.g., Brandt 2018; Kervella et al. 2019), this rich resource will enable targeted searches for substellar companions to nearby young stars that are amenable to direct detection, spectroscopic characterization, and eventual dynamical mass measurements. The release of this catalog will be timely for the launch of the *James Webb Space Telescope*; the sensitivity of the thermal-infrared coronagraphic instruments will be sufficient to detect wide-orbit Jovians around much older (and typically closer) stars than have previously been targeted from the ground.

We are grateful to the referee who helped to improve the quality of this work. We thank Trent Dupuy for useful discussions relating to this work. Supported by NSF grants AST-1411868 (R.D.R., E.L.N., K.B.F., B.M., J.P., and J.H.), AST-141378 (G.D.), and AST-1518332 (R.D.R., J.J.W., T.M. E., J.R.G., and P.G.K.). Supported by NASA grants NNX14 AJ80G (R.D.R., E.L.N., B.M., F.M., and M.P.), NSSC17K0535 (R.D.R, E.L.N., B.M., and J.B.R.), and NNX15AC89G and NNX15AD95G (R.D.R., B.M., J.E.W., T.M.E., G.D., J.R.G., and P.G.K.). This work benefited from NASA's Nexus for Exoplanet System Science (NExSS) research coordination network sponsored by NASA's Science Mission Directorate. J.R. is supported by the French National Research Agency in the framework of the Investissements d'Avenir program (ANR-15-IDEX-02) through the funding of the "Origin of Life" project of the University Grenoble-Alpes. Portions of this work were performed under the auspices of the U.S. Department of Energy by Lawrence Livermore National Laboratory under contract DE-AC52-07NA27344. V.P.B. acknowledges government sponsorship. Portions of this work were carried out at the Jet Propulsion Laboratory, California Institute of Technology, under a contract

with the National Aeronautics and Space Administration. J.J.W. is supported by the Heising-Simons Foundation 51 Pegasi b postdoctoral fellowship. Based on observations obtained at the Gemini Observatory, which is operated by the Association of Universities for Research in Astronomy, Inc., under a cooperative agreement with the NSF on behalf of the Gemini partnership: the National Science Foundation (United States), National Research Council (Canada), CONICYT (Chile), Ministerio de Ciencia, Tecnología e Innovación Productiva (Argentina), Ministério da Ciência, Tecnologia e Inovação (Brazil), and Korea Astronomy and Space Science Institute (Republic of Korea). This research used resources of the National Energy Research Scientific Computing Center, a DOE Office of Science User Facility supported by the Office of Science of the U.S. Department of Energy under contract No. DE-AC02-05CH11231. This work used the Extreme Science and Engineering Discovery Environment (XSEDE), which is supported by National Science Foundation grant No. ACI-1548562. This work has made use of data from the European Space Agency (ESA) mission *Gaia* (https://www.cosmos.esa.int/gaia), processed by the *Gaia* Data Processing and Analysis Consortium (DPAC; https://www.cosmos.esa.int/web/gaia/dpac/consortium). Funding for the DPAC has been provided by national institutions, in particular the institutions participating in the *Gaia* Multilateral Agreement. This research has made use of the SIMBAD database and the VizieR catalog access tool, both operated at the CDS, Strasbourg, France. This research has made use of the Washington Double Star Catalog maintained at the U.S. Naval Observatory.

Facility: Gemini:South (GPI).

Software: Astropy (The Astropy Collaboration et al. 2013), Matplotlib (Hunter 2007), pyKLIP (Wang et al. 2015).

ORCID iDs

Robert J. De Rosa https://orcid.org/0000-0002-4918-0247
Eric L. Nielsen https://orcid.org/0000-0001-6975-9056
Jason J. Wang https://orcid.org/0000-0003-0774-6502
S. Mark Ammons https://orcid.org/0000-0001-5172-7902
Gaspard Duchêne https://orcid.org/0000-0002-5092-6464
Bruce Macintosh https://orcid.org/0000-0003-1212-7538
Julien Rameau https://orcid.org/0000-0003-0029-0258
Vanessa P. Bailey https://orcid.org/0000-0002-5407-2806
Travis Barman https://orcid.org/0000-0002-7129-3002
Joanna Bulger https://orcid.org/0000-0003-4641-2003
Jeffrey Chilcote https://orcid.org/0000-0001-6305-7272
Tara Cotten https://orcid.org/0000-0003-0156-3019
Thomas M. Esposito https://orcid.org/0000-0002-0792-3719
Michael P. Fitzgerald https://orcid.org/0000-0002-0176-8973
Katherine B. Follette https://orcid.org/0000-0002-7821-0695
Benjamin L. Gerard https://orcid.org/0000-0003-3978-9195
Stephen J. Goodsell https://orcid.org/0000-0002-4144-5116
Alexandra Z. Greenbaum https://orcid.org/0000-0002-7162-8036
Pascale Hibon https://orcid.org/0000-0003-3726-5494
Li-Wei Hung https://orcid.org/0000-0003-1498-6088
Patrick Ingraham https://orcid.org/0000-0003-3715-8138
Quinn Konopacky https://orcid.org/0000-0002-9936-6285
James E. Larkin https://orcid.org/0000-0001-7687-3965
Franck Marchis https://orcid.org/0000-0001-7016-7277
Mark S. Marley https://orcid.org/0000-0002-5251-2943
Christian Marois https://orcid.org/0000-0002-4164-4182
Stanimir Metchev https://orcid.org/0000-0003-3050-8203
Maxwell A. Millar-Blanchaer https://orcid.org/0000-0001-6205-9233
Rebecca Oppenheimer https://orcid.org/0000-0001-7130-7681
David Palmer https://orcid.org/0000-0001-7128-0802
Marshall Perrin https://orcid.org/0000-0002-3191-8151
Abhijith Rajan https://orcid.org/0000-0002-9246-5467
Fredrik T. Rantakyrö https://orcid.org/0000-0002-9667-2244
Jean-Baptiste Ruffio https://orcid.org/0000-0003-2233-4821
Dmitry Savransky https://orcid.org/0000-0002-8711-7206
Adam C. Schneider https://orcid.org/0000-0002-6294-5937
Anand Sivaramakrishnan https://orcid.org/0000-0003-1251-4124
Inseok Song https://orcid.org/0000-0002-5815-7372
Remi Soummer https://orcid.org/0000-0003-2753-2819
Sandrine Thomas https://orcid.org/0000-0002-9121-3436
Kimberly Ward-Duong https://orcid.org/0000-0002-4479-8291
Sloane Wiktorowicz https://orcid.org/0000-0003-4483-5037
Schuyler Wolff https://orcid.org/0000-0002-9977-8255

References

Abt, H. A. 2005, ApJ, 629, 507
Abt, H. A., & Morrell, N. I. 1995, ApJS, 99, 135
Allard, F., Homeier, D., & Freytag, B. 2012, RSPTA, 370, 2765
Arenou, F., Luri, X., Babusiaux, C., et al. 2018, A&A, 616, A17
Baraffe, I., Chabrier, G., Barman, T. S., Allard, F., & Hauschildt, P. H. 2003, A&A, 402, 701
Bell, C. P. M., Mamajek, E. E., & Naylor, T. 2015, MNRAS, 454, 593
Beust, H., Augereau, J. C., Bonsor, A., et al. 2014, A&A, 561, 43
Brandt, T. D. 2018, ApJS, 239, 31
Brandt, T. D., Dupuy, T. J., & Bowler, B. P. 2019, AJ, 158, 140
Calissendorff, P., & Janson, M. 2018, A&A, 615, A149
Chilcote, J., Pueyo, L., De Rosa, R. J., et al. 2017, AJ, 153, 182
De Rosa, R. J., Nguyen, M. M., Chilcote, J., et al. 2019, arXiv:1910.08659
De Rosa, R. J., Nielsen, E. L., Blunt, S. C., et al. 2015, ApJL, 814, L3
Dupuy, T. J., Brandt, T. D., Kratter, K. M., & Bowler, B. P. 2019, ApJL, 871, L4
Feigelson, E. D., Lawson, W. A., Stark, M., Townsley, L., & Garmire, G. P. 2006, AJ, 131, 1730
Foreman-Mackey, D., Hogg, D. W., Lang, D., & Goodman, J. 2013, PASP, 125, 306
Fortney, J. J., Marley, M. S., Saumon, D., & Lodders, K. 2008, ApJ, 683, 1104
Gaia Collaboration, Brown, A. G. A., Vallenari, A., et al. 2018, A&A, 616, A1
Gaia Collaboration, Prusti, T., de Bruijne, J. H. J., et al. 2016, A&A, 595, A1
Hoffleit, D., & Jaschek, C. (ed.) 1991, The Bright Star Catalogue (5th; New Haven, CT: Yale Univ. Observatory)
Hunter, J. D. 2007, CSE, 9, 90
Kervella, P., Arenou, F., Mignard, F., & Thévenin, F. 2019, A&A, 623, A72
Lindegren, L., Hernández, J., Bombrun, A., et al. 2018, A&A, 616, A2
Macintosh, B., Graham, J. R., Barman, T., et al. 2015, Sci, 350, 64
Macintosh, B., Graham, J. R., Ingraham, P., et al. 2014, PNAS, 111, 12661
Maire, A. L., Rodet, L., Cantalloube, F., et al. 2019, A&A, 624, A118
Marley, M. S., Fortney, J. J., Hubickyj, O., Bodenheimer, P., & Lissauer, J. J. 2007, ApJ, 655, 541
Marois, C., Lafrenière, D., Doyon, R., Macintosh, B., & Nadeau, D. 2006, ApJ, 641, 556
Mason, B. D., Wycoff, G. L., Hartkopf, W. I., Douglass, G. G., & Worley, C. E. 2001, AJ, 122, 3466
Nielsen, E. L., De Rosa, J. R., & Wang, J. J. 2019b, AJ, submitted
Nielsen, E. L., De Rosa, R. J., Macintosh, B., et al. 2019a, AJ, 158, 13
Nielsen, E. L., De Rosa, R. J., Wang, J., et al. 2016, AJ, 152, 175
Nielsen, E. L., Liu, M. C., Wahhaj, Z., et al. 2013, ApJ, 776, 4
Perrin, M. D., Maire, J., Ingraham, P., et al. 2014, Proc. SPIE, 9147, 91473J
Perryman, M., Hartman, J., Bakos, G. Á., & Lindegren, L. 2014, ApJ, 797, 14
Pourbaix, D., Tokovinin, A. A., Batten, A. H., et al. 2004, A&A, 424, 727
Pueyo, L., Soummer, R., Hoffmann, J., et al. 2015, ApJ, 803, 31
Rajan, A., Rameau, J., De Rosa, R. J., et al. 2017, AJ, 154, 10
Sahlmann, J., Segransan, D., Queloz, D., et al. 2010, A&A, 525, A95
Simon, M., & Schaefer, G. H. 2011, ApJ, 743, 158
Snellen, I. A. G., Brandl, B. R., de Kok, R. J., et al. 2014, Natur, 509, 63

Snellen, I. A. G., & Brown, A. G. A. 2018, NatAs, 2, 883
Soummer, R., Pueyo, L., & Larkin, J. 2012, ApJL, 755, L28
The Astropy Collaboration, Robitaille, T. P., Tollerud, E. J., et al. 2013, A&A, 558, A33
van Leeuwen, F. 2007a, A&A, 474, 653
van Leeuwen, F. 2007b, Hipparcos, the New Reduction of the Raw Data (Dordrecht: Springer)
Wang, J., Mawet, D., Ruane, G., Hu, R., & Benneke, B. 2017, AJ, 153, 183
Wang, J. J., Graham, J. R., Dawson, R., et al. 2018a, AJ, 156, 192
Wang, J. J., Graham, J. R., Pueyo, L., et al. 2016, AJ, 152, 97
Wang, J. J., Perrin, M. D., Savransky, D., et al. 2018b, JATIS, 4, 018002
Wang, J. J., Rajan, A., Graham, J. R., et al. 2014, Proc. SPIE, 9147, 914755
Wang, J. J., Ruffio, J.-B., De Rosa, R. J., et al. 2015, pyKLIP: PSF Subtraction for Exoplanets and Disks, Astrophysics Source Code Library, ascl:1506.0011
Zuckerman, B., Song, I., Bessell, M. S., & Webb, R. A. 2001, ApJL, 562, L87